Three–dimensional acoustic imaging using asynchronous microphone array measurements

Merino Martinez, R.; von den Hoff, B.; Morata, David; Snellen, M.

Publication date
2022

Document Version
Final published version

Published in
9th Berlin Beamforming Conference 2022

BeBeC-2022-S08

THREE–DIMENSIONAL ACOUSTIC IMAGING USING ASYNCHRONOUS MICROPHONE ARRAY MEASUREMENTS

Roberto Merino-Martínez[1], Bieke von den Hoff[1], David Morata[2], and Mirjam Snellen[1]

[1]Faculty of Aerospace Engineering, Delft University of Technology.
Kluyverweg 1, 2629 HS Delft, The Netherlands.

[2]University of California, Irvine
Irvine, 92697, California, USA.

Abstract

Complex test models in aeroacoustic experiments often present an arrangement of noise sources within a three–dimensional space. Planar microphone array normally have difficulties in separating sound sources in the direction normal to the array plane due to their poorer spatial resolution in this direction. This paper evaluates the benefits of combining asynchronous microphone array measurements for three–dimensional acoustic source. An experimental setup consisting of three out–of–plane speakers was considered. A planar microphone array was employed for the acoustic measurements in a baseline position and then displaced around the speakers to provide different points of view. The acoustic source maps obtained from each array position were combined using the geometric mean of their source autopowers. The performance of this approach in combination with the following acoustic imaging methods was investigated: conventional frequency domain beamforming (as baseline), functional beamforming, orthogonal beamforming, robust adaptive beamforming, CLEAN–SC, Richardson–Lucy deconvolution, and global optimization methods. For each case, the performance is evaluated in terms of accuracy in source position localization and spectral quantification in sound pressure level. In general, it was determined that combining additional views considerably improved the accuracy in terms of position localization (especially in the depth direction).

1 INTRODUCTION

Noise emissions are a critical aspect for the social acceptance of several industrial systems, such as aircraft [1–3], wind turbines [4, 5], ground vehicles [6, 7], and rotating machinery

[8, 9]. Due to its negative effects on health and well–being, noise exposure in communities is typically limited by strict environmental laws [10]. Most industrial systems typically encompass complicated distributions of multiple noise sources and, to study and mitigate the noise levels emitted, it is of paramount importance to accurately determine the location and strength of the individual noise sources [11]. To achieve this purpose, phased microphone arrays [12, 13] combined with acoustic imaging algorithms [14, 15] are often employed.

The performance (especially in terms of spatial resolution and presence of sidelobes, i.e. spurious sources) of this approach strongly depends on the number of microphones within the array and their spatial distribution [12, 13, 16]. In practice, the limited number of microphones N available in the array (usually due to practical or budgetary reasons), restricts the array capabilities and design and a compromise solution is usually sought for achieving an acceptable spatial resolution (requiring arrays with large aperture) and sidelobe level (requiring densely populated arrays) values [16, 17]. Most experimental facilities, such as aeroacoustic wind tunnels [18–25], usually employ planar microphone arrays [12], partly due to their simplicity in terms of design and setup, but also because of the typical use of planar scan grids parallel to the array plane which contain the expected locations of the sound sources of interest.

However, planar microphone arrays normally have a poor resolution in the normal direction to the array plane (i.e. depthwise) [26, 27], which hinders the mapping of sound sources in a three–dimensional domain. Hence, the identification of sound sources in the normal direction to the array's plane is particularly difficult [28]. Nevertheless, three–dimensional (3D) acoustic source mapping is gaining interest lately for the study of complex sound source arrangements, such as aircraft components [9, 29], airfoils [27, 30], and passenger vehicles [20, 28, 31]. It should be noted that three–dimensional acoustic source mapping requires a considerably larger computational time due to the typically higher number of grid points and an adapted formulation of the acoustic imaging algorithm [32–36].

An option to overcome the poor depth resolution limitation to some extent is to use three–dimensional microphone arrays [37, 38] or several planar microphone arrays placed in different planes synchronously [9, 27, 34, 36, 39]. Nevertheless, this approach leads to a dedicated experimental setup, which normally implies a large value of N and a specific arrangement for the microphone positions. An alternative approach to additionally enhance the three–dimensional acoustic source maps is to virtually increase N by combining the results of multiple asynchronous microphone array measurements, in which the sound source remains at the same location but the microphone array is displaced to different positions to obtain different points of view [40–45]. In this way, higher spatial sampling is obtained. The sound field needs to have quasi–stationarity and ergodicity, i.e. the sound emissions should not vary with time [46], and the distance between the microphone array and the sound source should be small enough so that the wavefronts still have some curvature instead of being considered as plane waves. This approach benefits from the fact that the sidelobe pattern of the array and main beam pattern (i.e. the point spread function, PSF [12]) are strongly dependent on the relative location between the sound source considered and the microphone array. Therefore, measurements using different array locations will present different beam patterns, which can be exploited to further improve the quality of the source maps.

This paper investigates the use of multiple asynchronous measurements with a planar array (normally called prototype array) placed at different positions to improve the standard results obtained with a single measurement for three–dimensional source mapping applications.

A sound source arrangement featuring three different speakers emitting incoherent broadband noise was considered. A motivation for this research is that, as aforementioned, a large number of experimental facilities are equipped with (at least) a single planar microphone array that can be easily displaced within the measurement room and could benefit from this approach without increasing their cost. In this study, the microphone distribution of the prototype microphone array is kept constant to reduce the operational time required. In particular, the performance of several advanced acoustic imaging methods [21, 47–51] applied to a combination of asynchronous microphone array measurements is assessed. This analysis can be considered as an extension of a recently published study [45] that assessed combinations of asynchronous microphone array measurements, but only using the conventional beamforming algorithm [52].

The acoustic imaging methods considered are briefly introduced in section 2, as well as the techniques to combine different acoustic source maps obtained from asynchronous microphone array measurements. The experimental setup employed is described in section 3. The results obtained are discussed in section 4 and the main conclusions are drawn in section 5.

2 ACOUSTIC IMAGING METHODS

2.1 Conventional frequency domain beamforming (CFDBF)

Conventional frequency domain beamforming (CFDBF) [52] is a method based on the phase differences between the signals recorded by each microphone of the array. This technique considers a discretized scan grid of potential sound sources and performs an exhaustive search: for each grid point, the agreement between the expected solution for a potential sound source at that location and the actual signals recorded by the array microphones is assessed. In essence, this process is a directional scanning and the outcome is maximum when a focal position coincides with the location of the actual sound source and smaller elsewhere [52]. This method is widely–used since it is robust, intuitive, and relatively computationally inexpensive. However, CFDBF is influenced by the array's PSF, i.e. the array's response to a unitary point source, which is limited by the Rayleigh resolution limit, i.e. the minimum distance at which two sound sources can be distinguished, and is subject to high sidelobe levels (spurious sources), especially at high frequencies.

2.2 Functional beamforming (FUNBF)

Functional beamforming (FUNBF) [53] provides a higher dynamic range (or lower sidelobe level) and narrower main lobes than CFDBF. In essence, this technique consists in raising the autopowers of the CFDBF source map (see section 2.1) to the power of an exponent parameter ν and the cross–spectral matrix (CSM) [12] to the inverse of this power $1/\nu$. In theory, the higher the value of ν, the higher the dynamic range obtained. However, in practice, FUNBF has a relatively high sensitivity to errors made in the steering vectors of the scan grid points, in case these do not precisely match the exact position of the actual sound source. This sensitivity can cause considerably lower quantitative predictions at high frequencies, especially, if coarse grids and high values of ν are employed [50]. For this paper, the value of ν was selected to be 8 after performing a sensitivity analysis [54, 55].

2.3 Orthogonal beamforming (OB)

Orthogonal beamforming (OB) [56] is based on the eigenvalue decomposition of the CSM. It is based on the idea of separating the signal (incoherent sound sources) and the noise (non–acoustic pressure fluctuations) subspaces. OB considers a matrix G consisting of the steering vectors between the incoherent sound sources and the array microphones. The main idea behind OB is that each eigenvalue of G can be used to estimate the absolute source level of one source, from the strongest sound source within the map to the weakest, assuming orthogonality between steering vectors. These sources are then mapped to specific locations by assigning the eigenvalues to the location of the highest peak in a beamforming source map constructed from a rank–one CSM synthesized from the corresponding eigenvector. An important parameter, which has to be adjusted by the user, is the number of eigenvalues that span the signal subspace, which can be estimated by observing the number of dominant eigenvalues of the CSM. In this paper, the number of eigenvalues was defined in a flexible way as those whose sum contains 90% of the trace of the matrix.

2.4 Robust adaptive beamforming (RAB)

Adaptive beamforming (AB) [57, 58], also known as Capon or minimum variance distortionless response (MVDR) beamforming, can provide acoustic images with a higher spatial resolution than CFDBF and has mostly been used in array signal processing for sonar and radar applications. This method employs a weighted steering vector formulation based on the inverse of the CSM that maximizes the signal–to–noise ratio (SNR). Despite its super–resolution, AB is relatively sensitive to any perturbations and its performance quickly deteriorates below an acceptable level, preventing its direct application for aeroacoustic measurements [59]. To overcome this issue, a robust adaptive beamforming (RAB) variation was proposed [59] specifically for aeroacoustic applications. To mitigate any potential ill–conditioning of the CSM, diagonal loading [59] is applied. The optimal value of the diagonal loading factor ε_0 needs to be determined empirically. One method proposed by Huang et al. [59] consists of calculating the largest eigenvalue σ of the CSM and multiplying it by a diagonal loading parameter μ_0. In general, smaller values of μ_0 provide acoustic images with better array resolution but the computation can fail due to numerical instability. On the other hand, a larger value of μ_0 generates closer results to the CFDBF. Typical values of μ_0 normally range between 0.001 and 0.5. For this research a value of $\mu_0 = 0.1$ was selected after a sensitivity analysis [55].

2.5 CLEAN-SC

CLEAN–SC [60] is a deconvolution technique that uses the fact that sidelobes are spatially coherent with the main lobe [60]. CLEAN–SC is based on the assumption that the CSM can be written as a summation of contributions from incoherent sources. The CLEAN–SC algorithm starts by finding the steering vector yielding the maximum value of the CFDBF source map. The contribution of the source component corresponding to that steering vector is then multiplied by a loop gain factor $\tilde{\varphi}$ between 0 and 1 (selected as 0.99 in this paper [60]) and subtracted from the CSM and, afterward, the same procedure is repeated for the remaining CSM, until a certain stop criterion is fulfilled [60]. Ideally, the remaining CSM is "empty" after the iterative process. In other words, its norm should be small compared to the one of the original CSM.

The new source map is obtained by the summation of the clean beams of the identified sound sources and the remaining degraded CSM [16]. This method has a relatively low sensitivity to errors made in the source model that describe the sound propagation, i.e. if the steering vectors considered do not exactly match with the source vectors [61].

2.6 Richardson–Lucy deconvolution (RL)

The Richardson–Lucy (RL) deconvolution approach is a Bayesian–based technique that works in the frequency domain. The method originated within the field of astronomy [62, 63] and has been adapted and extensively used in acoustic beamforming during the past years [64–68]. This technique associates the PSF with the concept of conditional probability. Inversion of the acoustic integral makes use of Bayes' theorem to find the inverse conditional probability of the PSF. Similar to other popular deconvolution techniques, such as DAMAS [69], the RL approach requires the prior computation of the acoustic source map obtained by CFDBF and knowledge about the PSF, to then attempt at separating the contributions of the PSF from the CFDBF map to find the real source distribution. It presents several advantages when compared to the DAMAS Gauss–Seidel algorithm, as the output does not depend on the sequence order of equations. In addition, the rendering of distributed sound sources obtained with RL appears to be smoother when compared to DAMAS, in which the source has a speckle–like nature in many instances [65, 70], and is inherently positive (no need to enforce non–negativity of the source autopowers). However, the method can become computationally demanding on a three–dimensional scan grid. To alleviate the computational cost, this study approximates the PSF as shift–invariant PSF for every array plane. The focal point was selected to be $(x,y,z) = (0,0,-2.32)$ m.

2.7 Global optimization methods (GO)

The search for the locations and amplitudes of sound sources in a three–dimensional space can be considered a global optimization (GO) problem [35]. This method is essentially grid–free and has proven to overcome the Rayleigh resolution limit [71]. Differential evolution algorithms can be employed for the global optimization to escape local optima, such as sidelobes [35]. These optimization methods mimic natural evolution by using populations of solutions, where promising solutions are given a high probability to reproduce and worse solutions have a lower probability to reproduce. Estimates for source positions and source strengths are obtained as a potential solution to the optimization and do not need to be obtained from a source map. The number of sound sources present is typically not known *a priori*, but a simple iterative process can be performed using as a first guess the number of dominant eigenvalues of the CSM. By minimizing an objective function defined as the difference between the modeled CSM and the measured CSM, the solution will converge over several generations to the actual position and strength of the sound sources. For this study, the setting parameters required for the GO method [35] were a population size q of 64, a multiplication factor F of 0.6, and a crossover probability p_C of 0.75. A total of 5 independent runs were performed, each of them with 600 generations. The GO method does not provide source maps like the other acoustic imaging methods explained above, but instead, energy landscapes for each variable searched (in this case the three coordinates (x,y,z) and the strength per sound source. These are not shown in this paper for brevity reasons, but the interested reader is referred to [35] for examples of these energy landscapes. A recent study [71] assessed the use of GO techniques for three–

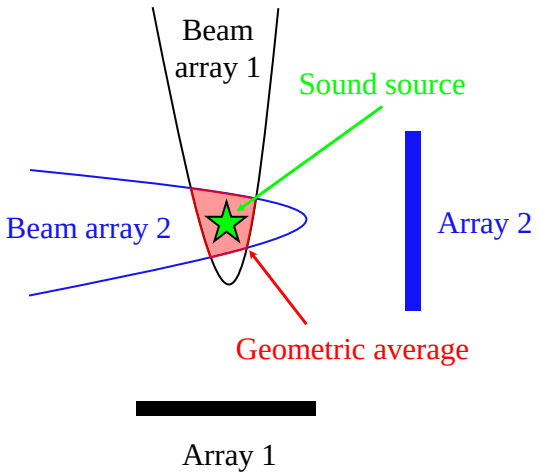

Figure 1: Diagram explaining the geometric average approach to combine two different acoustic source maps from asynchronous measurements taken by Array 1 and Array 2.

dimensional mapping of acoustic sources using the same experimental setup from section 3 with a single microphone array view (i.e. without combining asynchronous measurements). The results presented here are those adapted from [71].

2.8 Combination of asynchronous microphone array measurements

Once these methods have been applied to the acoustic data recorded by the microphone array placed in different positions (see Fig. 2c), the individual acoustic source maps obtained in each asynchronous measurement can be combined to improve the quality of the results obtained [45]. Especially, the resolution in the direction perpendicular to the array plane is expected to improve by combining measurements from different points of view. Figure 1 shows an example of the typical beam patterns of two perpendicular arrays (elongated in the direction perpendicular to the array plane). In case the results of both arrays are combined using, for example, the geometrical average of the source autopowers in the grid, the end result will look something similar to the intersection of both beams (shaded in red in Fig. 1).

Several combination approaches have been considered in the literature [42, 45], such as the arithmetic mean of the source autopowers of each acoustic source map, their geometric mean, or simply taking the minimum value of all source maps, in order to reduce sidelobes even further [28]. The minimum value approach showed promising results in a recent study [45] that considered omnidirectional sources, but in case directional sources are employed, such as the current speakers (see their directivity pattern in Fig. 3f), it can lead to misleading results. Therefore, in the current study, the geometric mean of the individual acoustic source maps obtained from the different points of view of the array is employed.

Other alternatives for combining asynchronous microphone array measurements are based in building a larger CSM that consists of the CSMs of each of the N_m asynchronous measurements (or array views as denoted in this paper) considered [45] and that has a total size of $(NN_\mathrm{m}) \times (NN_\mathrm{m})$. The CSMs of the N_m measurements are arranged in block diagonal positions and the remaining positions (i.e. the cross–correlations between pairs of microphones from

different measurements) are padded by zero elements, due to the lack of information relating different asynchronous measurements. This zero–padding poses a loss of information that synchronous measurements would not suffer. Recent studies have investigated the possibility of reconstructing the elements of the data-missing CSM [43, 44, 46, 70, 72]. These processes often require several assumptions about the characteristics of the acoustic sources, such as their sparsity [43] or the SNR [46]. The present work has investigated the possibility of completing the data–missing CSM (i.e. the block–Hermitian matrix resulting from the three array views) using a fast iterative shrinkage–thresholding algorithm (FISTA) minimization approach similar to that of Yu *et al.* [73]. The spatial basis was constructed by using a dimension–reduced Fourier space. The technique has been successfully applied in the past in the imaging of synthetic noise sources [73], industrial machinery [43, 73], and laboratory–scale supersonic jets [70]. However, efforts to complete the CSM in the present study were unsuccessful. This has been attributed to the large distance between the distinct array view angles (see Fig. 2c). The average distance between non–synchronous microphone pairs must be of the order of the correlation length scale for the frequencies of interest, a condition that was not fulfilled in the current experimental setup. As such, the completion of the CSM was penalized and the results were essentially similar to those obtained using the zero–padded block–Hermitian matrix.

3 EXPERIMENTAL SETUP

The experiments were performed inside the anechoic chamber of the Faculty of Applied Sciences at Delft University of Technology. The room has a cubic shape of 8 m $\times$ 8 m $\times$ 8 m and all walls, floor, and ceiling are covered with 1 m long glass wool wedges, which provides free–field sound propagation conditions (i.e. no sound reflections) for frequencies higher than 100 Hz, see Fig. 2a. The chamber is entirely decoupled from the building and has its own support, creating a fully vibration– and (virtually) background sound–free room (see background noise spectrum in Fig. 2e, which is likely conditioned by the measurement floor of the MEMS microphones used in the measurement). There is no structural floor present, instead, there is a wire net on which a rigid floor can be installed if required. The microphone array was placed on top of a small grid used as a rigid floor to support the tripod of the microphone array, see Fig. 2a. The current experimental setup was also employed for another study investigating the performance of global optimization methods for acoustic source mapping [71].

The phased microphone array employed was a CAE Systems Bionic M–112 microphone array [75] of 1 m in diameter consisting of 112 MEMS digital microphones. The microphone distribution of the prototype array is presented in Fig. 2b. The prototype array in its baseline position (see black dots Fig. 2c) was placed 2.32 m away from the second speaker (S2), the array's center aligned with the center of the baffle of S2. In the coordinate system considered, the prototype array is located in the $z = -2.32$ m plane. To provide different view angles to later combine as asynchronous measurements, the prototype array was rotated 90° and -90° along a rotation axis parallel to the y axis and located 0.21 m behind S2 (i.e. at $z = 0.21$ m). The rotated arrays are depicted in Fig. 2c as blue and red dots for the 90° and -90° rotations, respectively. A top view of the experimental setup is presented in Fig. 2d to observe the relative positions of the speakers in a better way. Each microphone within the array was calibrated following the guidelines of Mueller [11]. One microphone was found to be ill–performing and, hence, was not considered for the post–processing. The sampling frequency was 48 kHz and the recording

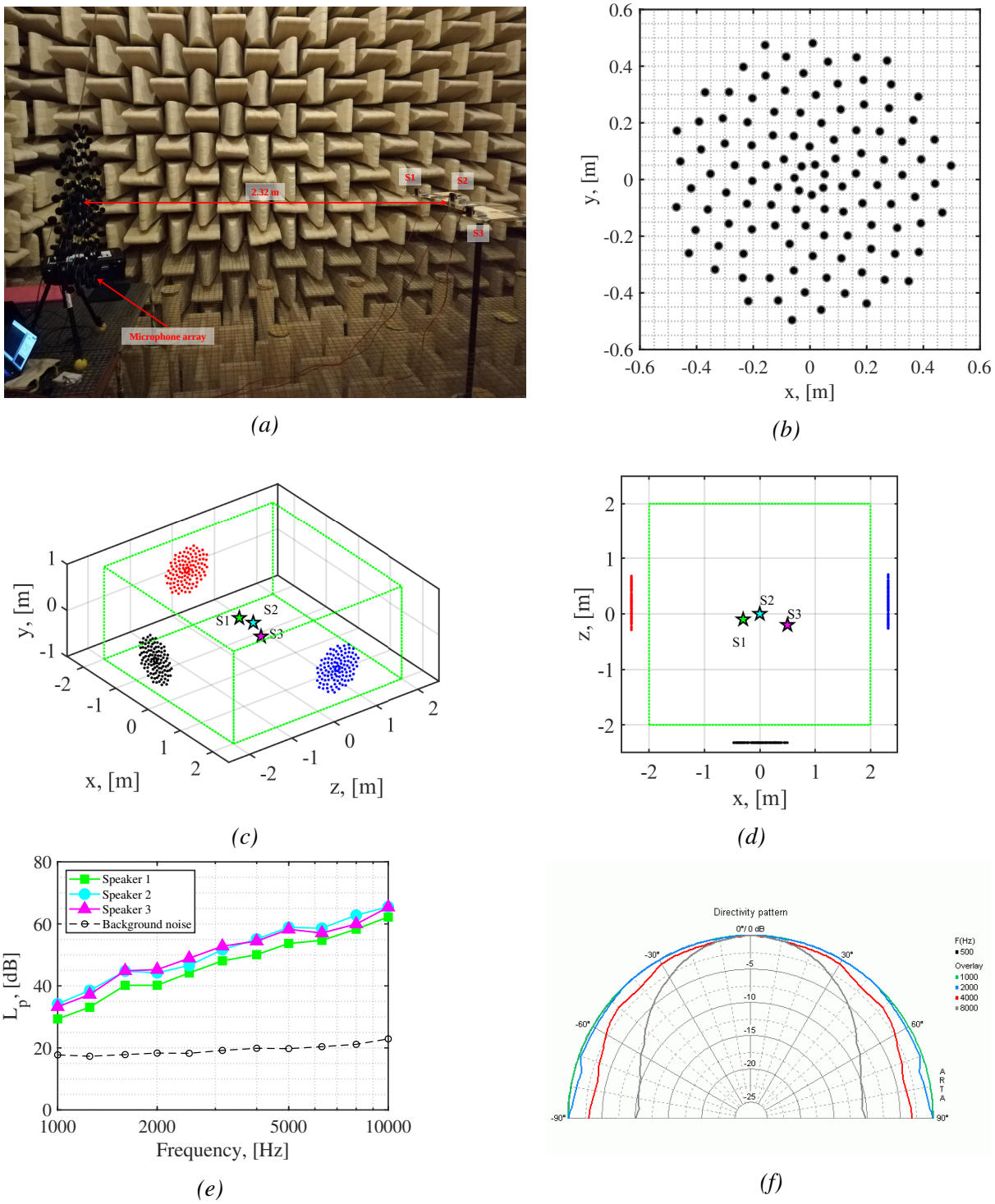

Figure 2: (a) Experimental setup inside of the anechoic chamber. (b) Microphone distribution of the prototype array (seen from behind). (c) Three–dimensional view of the prototype array (black dots) as well as those rotated 90° (blue dots) and −90° (red dots). The three speakers (S1–S3) are depicted as stars and the dotted green lines denote the boundaries of the scan grid. (d) Top view of the experimental setup. (e) Frequency spectra of each speaker measured 1 m in front of their baffle. (f) Directivity patterns of the speaker for different frequencies [74].

time was 15 s per measurement. For all acoustic imaging methods, the CSM is calculated using 4096 samples with a 50% overlap using Hanning windowing. Thus, the resulting frequency resolution is approximately 23.4 Hz.

Three Visaton FRWS 5 – 8 ohm speakers [74] were employed as reference sound sources, coupled to an amplifier and emitting incoherent broadband noise (see Fig. 2e). The speakers have a baffle diameter of 45 mm and an effective piston area of 12.5 cm^2. Their frequency responses range between 250 Hz and 10 kHz and they have a maximum power of 3 W. The directivity patterns of the speaker for different frequencies (500 Hz, 1 kHz, 2 kHz, 4 kHz, and 8 kHz) are depicted in Fig. 2f. The speakers were placed in front of the prototype array, on a wooden bar with a support system that did not require a rigid floor, see Fig. 2a. The relative positions (S1, S2, and S3 for speakers 1, 2, and 3, respectively) are depicted in Figs. 2c and d as a three–dimensional view and top view of the experimental setup, respectively. The center of the coordinate system considered is defined at the location of S2 (i.e. S2's coordinates are $(x,y,z) = (0,0,0)$ m), with the x axis pointing to the right as seen from the prototype array, the y axis in the vertical direction pointing up, and the z axis in the normal direction of the prototype array pointing away from it, see Fig. 2c. The coordinates of the other two speakers are $(x,y,z) = (-0.3,0,-0.1)$ m) for S1 and $(x,y,z) = (0.5,0,-0.2)$ m) for S3. As aforementioned, in this coordinate system, the center of the prototype array is located at $(x,y,z) = (0,0,-2.32)$ m, i.e. 2.32 m away from S2. Therefore, all speakers are contained in the $y = 0$ m plane. For the current experimental setup, the frequency corresponding to the Rayleigh resolution limit after which the prototype array is expected to be able to separate all the three sound sources is 3236 Hz. The sound spectra emitted by each speaker (with only one speaker emitting sound at a time) measured 1 m in front of their baffle are depicted in Fig. 2e with the background noise spectrum as reference. The overall sound pressure level $L_{\text{p,overall}}$ in the frequency range of 1 kHz to 10 kHz was 64.9 dB, 68.8 dB, and 67.9 dB, for speakers 1, 2, and 3, respectively. Table 1 provides an overview of the positions and $L_{\text{p,overall}}$ of each speaker. This combination of speakers aims at simulating a complex three–dimensional distribution of multiple closely–spaced noise sources, such as a landing gear system in aeroacoustic wind–tunnel experiments [23, 29, 76].

Table 1: Overview of the positions and overall sound pressure levels $L_{p,overall}$ between 1 kHz and 10 kHz for each speaker.

Speaker	Position (x,y,z), [m]	$L_{\text{p,overall}}$, [dB]
S1	(-0.3, 0, -0.1)	64.9
S2	(0, 0, 0)	68.8
S3	(0.5, 0, -0.2)	67.9

The three–dimensional scan grid employed ranges from -2 m to 2 m in x, from -1 m to 1 m in y, and from -2 m to 2 m in z, see the dotted green lines in Figs. 2c and d. A distance between grid points of $\Delta x = \Delta y = \Delta z = 0.01$ m was employed, i.e. a total of 32,321,001 scan grid points. Given its considerably higher computational cost, the grid for RL was smaller, ranging from -1 m to 1 m in x, from -0.2 m to 0.2 m in y, and from -1 m to 1 m in z and coarser, with a distance between grid points of $\Delta x = \Delta y = \Delta z = 0.05$ m, i.e. a total of 15,129 scan grid points.

The search space for GO (technically not a scan grid) ranged from -2 m to 2 m in x, from -2 m to 2 m in y, and from -2 m to 2 m in z.

4 RESULTS AND DISCUSSION

This section contains some exemplary acoustic source maps obtained by each acoustic imaging method considered for the one–third–octave frequency bands centered at 2.5 kHz and 5 kHz. The first case represents a frequency below the aforementioned frequency corresponding to the Rayleigh resolution limit of 3236 Hz, whereas the second case is above that limit. The three–dimensional acoustic source maps for the cases with a single view (prototype array at 0°), two views combined (0° and -90°), and all three views combined (0°, 90°, and -90°) are presented. All source maps are plotted as isocontours 3 dB (in red) and 6 dB (in yellow) below the peak value in the scan grid. As in Fig. 2c, the three speakers (S1–S3) are depicted as stars. To observe the results in a better way, they are presented in a smaller scan grid ranging from -1 m to 1 m in x, from -0.2 m to 0.2 m in y, and from -1 m to 1 m in z.

Figure 3 depicts the results obtained for CFDBF. As expected, the results with a single view (Figs. 3a and d) fail to properly localize the sound sources in the z direction given the planar array's poor depth resolution. The case with 2.5 kHz (Fig. 3a) is not able to separate S1 and S2 as different sources due to the limited spatial resolution in the x direction at that frequency. For 5 kHz (Fig. 3d), on the other hand, three different beams are shown, one for each speaker. Once the results of two views (Figs. 3b and e) or three views (Figs. 3c and f) are combined asynchronously, the accuracy in source localization in the z direction greatly improves and, for the case with 5 kHz (Figs. 3e and f), the three sources can be properly separated and localized. The combined results for 2.5 kHz (Figs. 3b and c) still show difficulties in separating S1 and S2 in the x direction due to the Rayleigh resolution limit. In general, adding a third view does not seem to change the acoustic source maps significantly for this case.

The relative errors for estimating the position and sound pressure level L_p of each speaker made by CFDBF in each case (a single view (0°), two views (0° and $-90°$) combined, and all the three views (0°, 90°, and $-90°$) combined) are calculated with respect to the reference values in Table 1 and the one–third–octave frequency band spectra in Fig 2e. The position and L_p of each speaker are estimated by searching for the peak L_p values in three subspaces: $x \leq -0.2$ m for S1, $-0.2\mathrm{m} < x \leq 0.35$ m for S2 and $x > 0.35$ m for S3. The errors in position ($\mathbf{x} = (x, y, z)$) are calculated as $\Delta\mathbf{x} = \mathbf{x}_\mathrm{estimated} - \mathbf{x}_\mathrm{ref}$, where $\mathbf{x}_\mathrm{estimated}$ and $\mathbf{x}_\mathrm{ref}$ are the estimated and reference position values, respectively. Similarly, the errors in sound pressure level are estimated as $\Delta L_\mathrm{p} = L_\mathrm{p,estimated} - L_\mathrm{p,ref}$, where $L_\mathrm{p,estimated}$ and $L_\mathrm{p,ref}$ are the estimated and reference sound pressure values, respectively. In addition, the absolute error averaged over the whole frequency range considered (the eleven one–third–octave bands between 1 kHz and 10 kHz) $\varepsilon = \overline{|\Delta L_\mathrm{p}|}$, i.e. the average $\mathscr{L}^1$ norm of the differences is depicted for each speaker in the legends.

The errors made by CFDBF are presented in Fig. 4 for the cases with one (a, d), two (b, e), and three views (c, f). As observed in the source maps of Fig. 3, the relative errors in the z direction are the largest for the case with a single view. The position errors considerably decrease if two or three views are employed. As explained before, the position errors below the frequency corresponding to the Rayleigh resolution limit increase due to the poor spatial resolution. The errors in L_p for the case with a single view (Fig. 4d) are relatively low and only increase below the Rayleigh resolution limit, especially for the weakest source (S1). The L_p

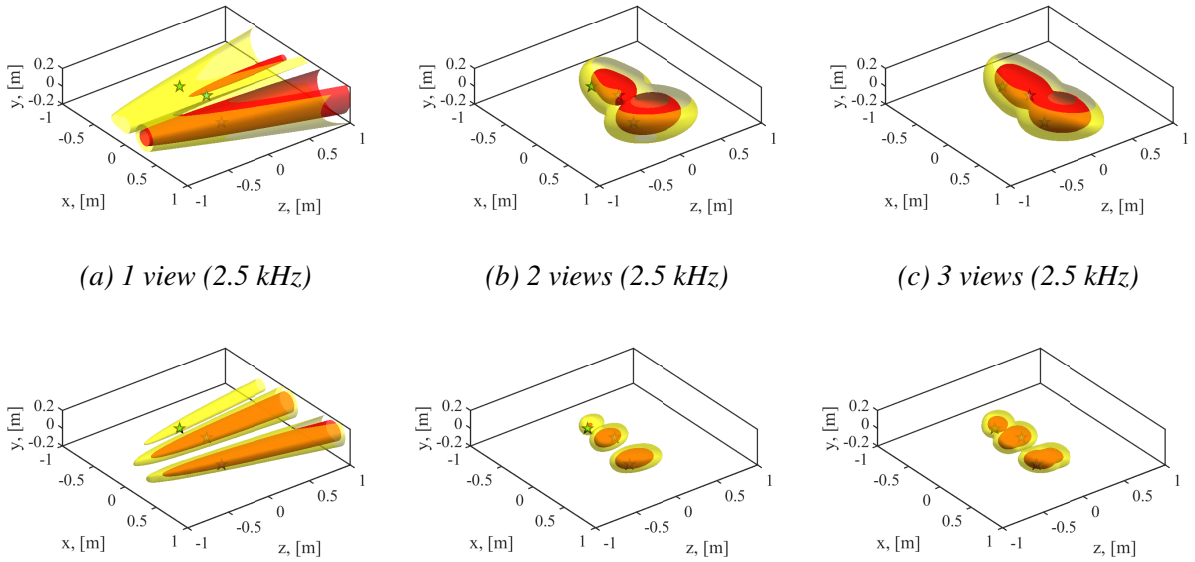

(a) 1 view (2.5 kHz) (b) 2 views (2.5 kHz) (c) 3 views (2.5 kHz)

(d) 1 view (5 kHz) (e) 2 views (5 kHz) (f) 3 views (5 kHz)

Figure 3: 3D acoustic source maps obtained for CFDBF for a one–third–octave frequency band centered at 2.5 kHz (first row) and 5 kHz (second row).

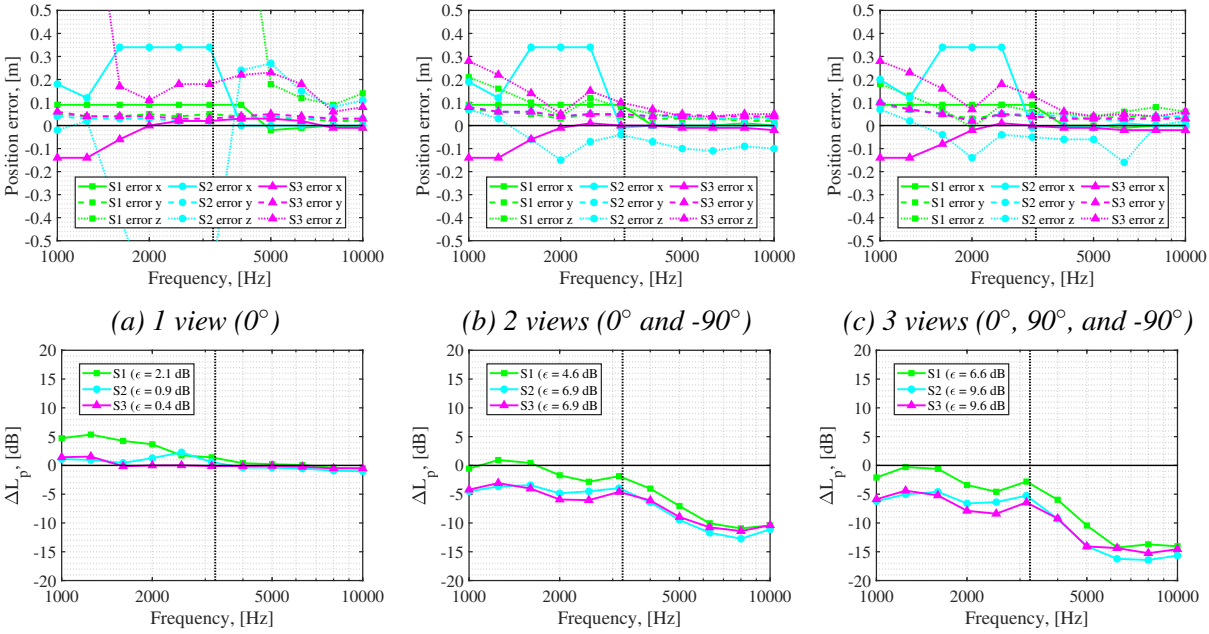

(a) 1 view (0°) (b) 2 views (0° and -90°) (c) 3 views (0°, 90°, and -90°)

(d) 1 view (0°) (e) 2 views (0° and -90°) (f) 3 views (0°, 90°, and -90°)

Figure 4: Relative errors in position in x, y, and z (first row) and L_p (second row) for each speaker made by CFDBF. The vertical dotted line represents the Rayleigh resolution limit.

errors for the cases with two and three views (Fig. 4e and f, respectively), considerably increase, especially for higher frequencies. This is partly explained by the stronger directionality pattern shown for higher frequencies in the emission directivity pattern of the speakers, see Fig. 2f. In fact, using three views instead of two further increases the estimation errors, which supports this idea.

The source maps obtained by FUNBF are presented in Fig. 5 for the same cases discussed above. In this case, the three speakers can be separated for the 2.5 kHz as three different beams (Fig. 5a). Once again, increasing the number of views enables a better localization in the z direction. In general, the case with 3 views (Fig. 5c) provides slightly wider lobes than the case with just 2 views (Fig. 5b). This is probably an artifact due to the directivity pattern of the sound sources, the application of the geometric mean approach, or uncertainties in the experimental setup.

The errors made by FUNBF are presented in Fig. 5. In general, the position errors are lower than those made by CFDBF and, in this case, the case with 3 views (Fig. 5c) notably reduces the error in the z position of S2 with respect to the case with only two views (Fig. 5b). On the other hand, the errors made for the L_p estimations are slightly higher than those for CFDBF, especially at higher frequencies, due to the aforementioned sensitivity of FUNBF when coarse grids are employed.

The results obtained by OB (Figs. 7 and 8) are essentially the same as those by CFDBF, since in a quiet environment without any other major sound sources present, they are expected to provide similar results for the parameters employed here [56]. Therefore, the same conclusions as for CFDBF apply.

The acoustic source maps obtained by RAB are presented in Fig. 9. The case with a single view (Fig. 9a and d) shows one distinct beam for each speaker (also for the 2.5 kHz band). However, there seems to be an offset in the location of the maxima in the positive z direction, which is also observed in the position error graphs in Fig. 10a. This method is probably the one that benefits the most from the combined approach with multiple asynchronous views because once two or three views are combined, the position errors (Figs. 10b and c) considerably decrease to similar levels as those made by FUNBF. The errors in L_p made by the single view case (Fig. 10d) are about 5 dB higher than those made by CFDBF, FUNBF, or OB. The quantification errors for the cases with two and three views (Fig. 10e and f), on the other hand, are slightly lower than the other methods.

The results obtained for CLEAN–SC are depicted in Figs. 11 and 12 for the acoustic source plots and the error graphs, respectively. Unlike in previous studies [29, 34] that also employed asynchronous microphone array measurements with CLEAN–SC for three–dimensional acoustic source mapping and achieved very successful results, the acoustic source maps obtained by CLEAN–SC in the current investigation seem to fail to properly identify the three different speakers as separate sound sources. Instead, in most cases, only S3 is identified (closest source to the prototype array), and with a positive offset in the z direction. Some source maps (such as the one–view case for 5 kHz for the prototype array, Fig. 11d) also identify S2, but the weakest source of all (S1) was not properly identified in this experiment. On the other hand, the source maps obtained for measurements with a single speaker emitting (not shown here for brevity reasons) did manage to identify the single sound source present in the three–dimensional space with relatively high accuracy. Therefore, the explanation for the poor performance of CLEAN–SC in the multi–source cases might be due to poor spatial resolution. The exact reasons for

this phenomenon are not yet known and are the subject of future work, such as extending the investigation of high–resolution versions of CLEAN–SC [16, 29, 61] to confirm this hypothesis. Given its poor source localization performance, the errors made by CLEAN–SC in terms of position and L_p (Fig. 12) are considerably larger than the other methods investigated.

The acoustic source maps provided by RL deconvolution (with a smaller and coarser grid, see section 3) are presented in Fig. 13. The cases for 2.5 kHz (Figs. 13a–c) seem to only identify two main distributed sound sources that get narrower around the actual speaker positions as the number of views employed increases from one to three. However, the spatial resolution obtained is not as high as some of the other methods presented before, such as FUNBF (see Figs. 5a–c). For the higher frequency case of 5 kHz, on the other hand, the speakers are properly identified once multiple views are employed (Figs. 13e and f), and the position errors are within once and twice the separation between scan points of the grid employed (0.05 m). The considerably higher computational cost of the RL deconvolution prevented a comparative study with the rest of the methods using the same scan grid and the number of frequencies analyzed. Therefore, no error graphs are shown for this method, and only the acoustic source maps are presented as indicative.

The outcome of GO methods is not technically a traditional acoustic source map, but rather the coordinates in (x, y, z) and the L_p for the number of sound sources the user requests the method to search for. Therefore, the results presented here for GO simply correspond to the error graphs in these variables (see Fig. 14 until the 6300 Hz one–third–octave frequency band for the case of a single view [71]). The position errors made by GO in x and y are considerably lower than those made by the other methods with a single view and of the same order as with the combined approach, likely due to the super–resolution offered by GO. There seems to be a consistent positive offset in the z coordinate estimated for the three speakers, as mentioned in [71]. The errors made in estimating L_p are of the same order as those made by CFDBF with a single view (see Fig. 4d), except for the lowest frequency band of 1 kHz that are somewhat higher. The asynchronous combination of additional views was investigated but did not improve the results obtained with a single view significantly. Future work might investigate the application of GO methods to the combined block–Hermitian CSM (consisting of the CSMs of different measurements) simultaneously, as explained in section 2.8.

It should be noted that the error results presented here were converted from errors expressed as narrowband spectra from [71] to one–third–octave band spectra by combining the narrowband errors within each band and calculating the average of their absolute value (i.e. the average $\mathscr{L}^1$ norm of the errors, similarly as done for the ε error parameters before). Therefore, this might influence the values presented here. Future comparisons should investigate calculating the one–third–octave error values directly from GO with multiple frequencies for a more fair comparison.

5 CONCLUSIONS

This paper has investigated the potential improvement of three–dimensional acoustic source mapping capabilities by combining asynchronous measurements of planar microphone arrays. This is especially interesting for test models featuring complicated arrangements of noise sources in 3D and for test facilities equipped with a planar microphone array that can be displaced around the test model. The performance of different acoustic imaging methods was

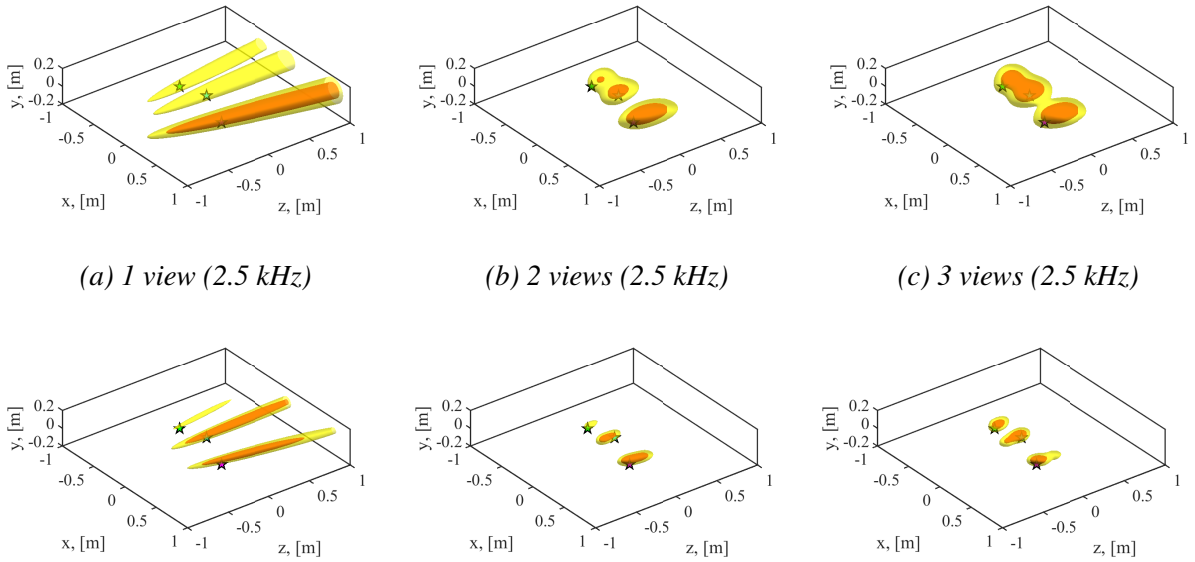

(a) 1 view (2.5 kHz) (b) 2 views (2.5 kHz) (c) 3 views (2.5 kHz)

(d) 1 view (5 kHz) (e) 2 views (5 kHz) (f) 3 views (5 kHz)

Figure 5: Three–dimensional acoustic source maps obtained for FUNBF for a one–third–octave frequency band centered at 2.5 kHz (first row) and 5 kHz (second row).

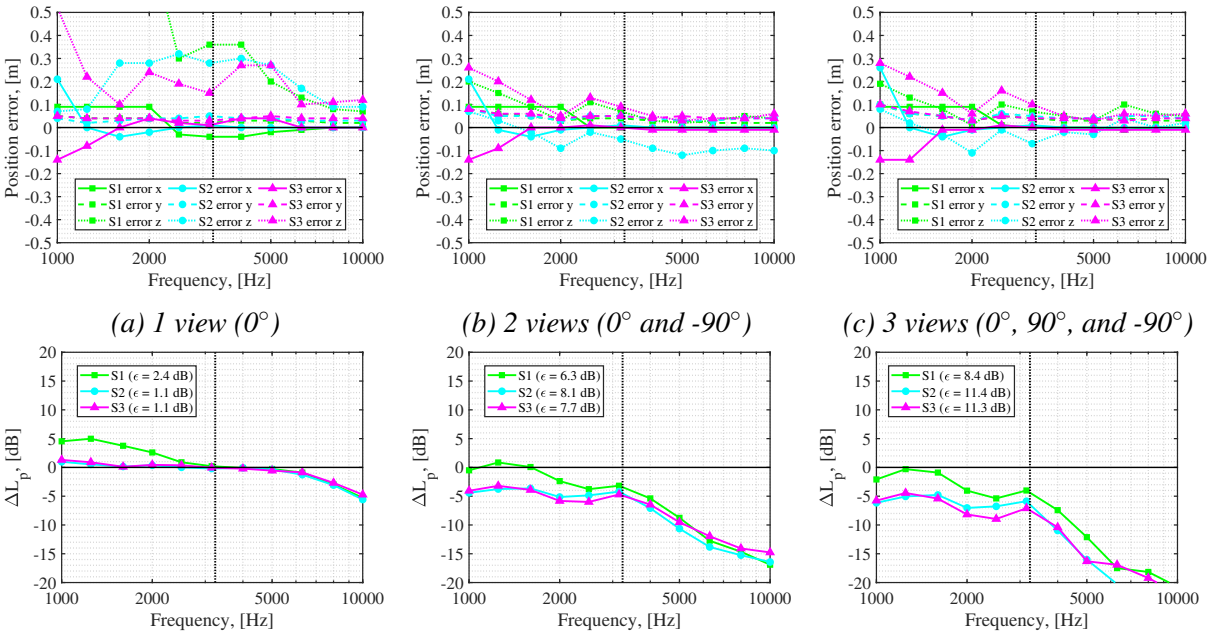

(a) 1 view (0°) (b) 2 views (0° and -90°) (c) 3 views (0°, 90°, and -90°)

(d) 1 view (0°) (e) 2 views (0° and -90°) (f) 3 views (0°, 90°, and -90°)

Figure 6: Relative errors in position in x, y, and z (first row) and L_p (second row) for each speaker made by FUNBF. The vertical dotted line represents the Rayleigh resolution limit.

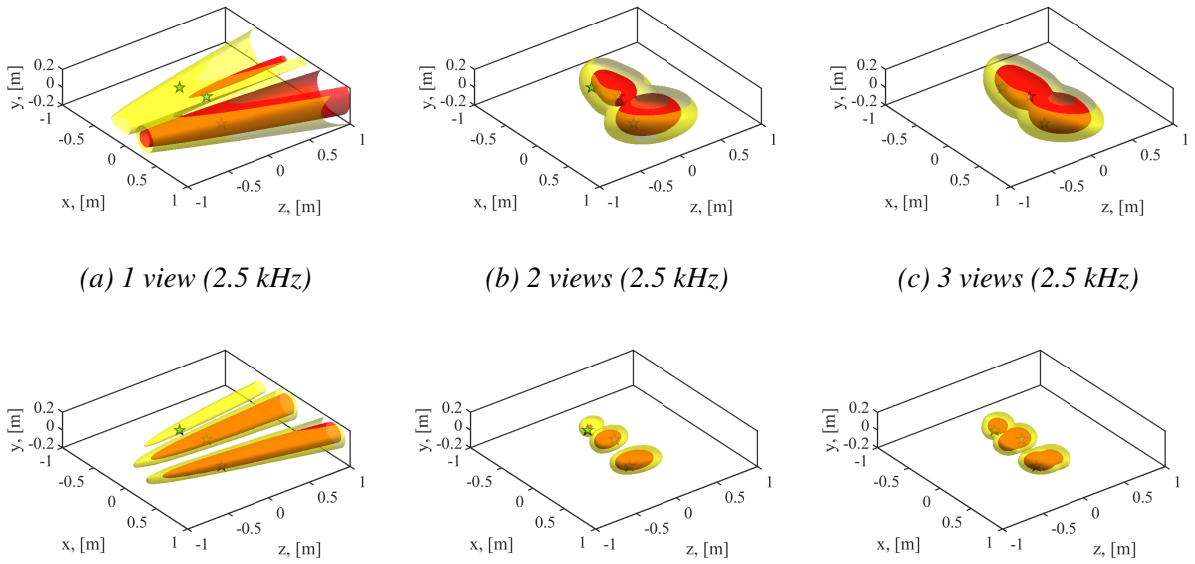

(a) 1 view (2.5 kHz) (b) 2 views (2.5 kHz) (c) 3 views (2.5 kHz)

(d) 1 view (5 kHz) (e) 2 views (5 kHz) (f) 3 views (5 kHz)

Figure 7: Three–dimensional acoustic source maps obtained for OB for a one–third–octave frequency band centered at 2.5 kHz (first row) and 5 kHz (second row).

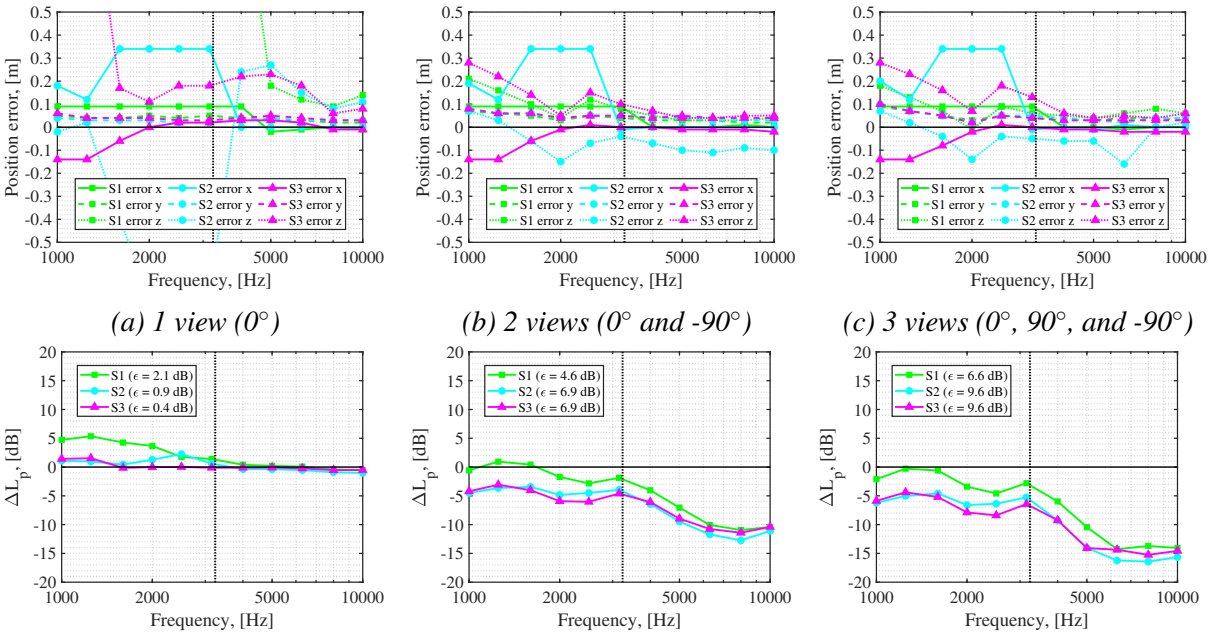

(a) 1 view (0°) (b) 2 views (0° and -90°) (c) 3 views (0°, 90°, and -90°)

(d) 1 view (0°) (e) 2 views (0° and -90°) (f) 3 views (0°, 90°, and -90°)

Figure 8: Relative errors in position in x, y, and z (first row) and L_p (second row) for each speaker made by OB. The vertical dotted line represents the Rayleigh resolution limit.

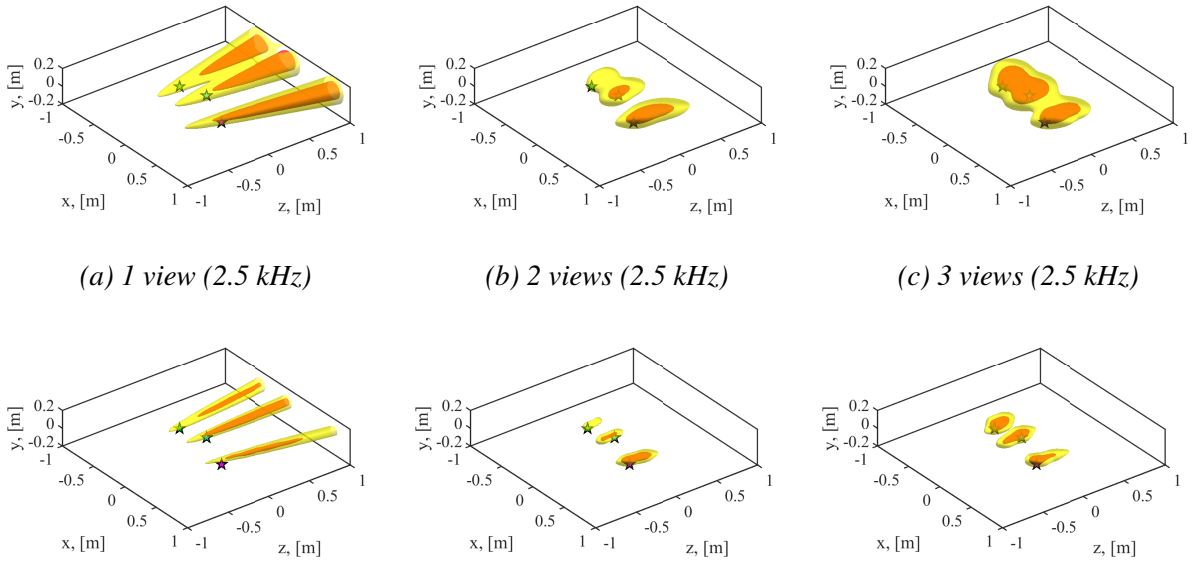

(a) 1 view (2.5 kHz) (b) 2 views (2.5 kHz) (c) 3 views (2.5 kHz)

(d) 1 view (5 kHz) (e) 2 views (5 kHz) (f) 3 views (5 kHz)

Figure 9: Three–dimensional acoustic source maps obtained for RAB for a one–third–octave frequency band centered at 2.5 kHz (first row) and 5 kHz (second row).

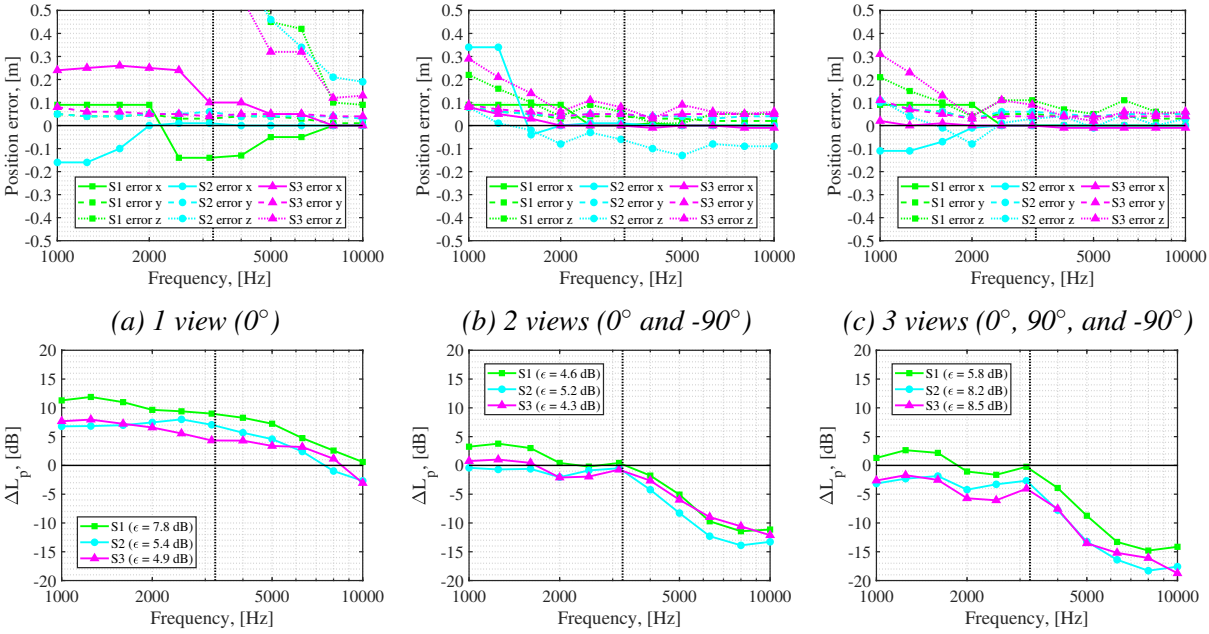

(a) 1 view (0°) (b) 2 views (0° and -90°) (c) 3 views (0°, 90°, and -90°)

(d) 1 view (0°) (e) 2 views (0° and -90°) (f) 3 views (0°, 90°, and -90°)

Figure 10: Relative errors in position in x, y, and z (first row) and L_p (second row) for each speaker made by RAB. The vertical dotted line represents the Rayleigh resolution limit.

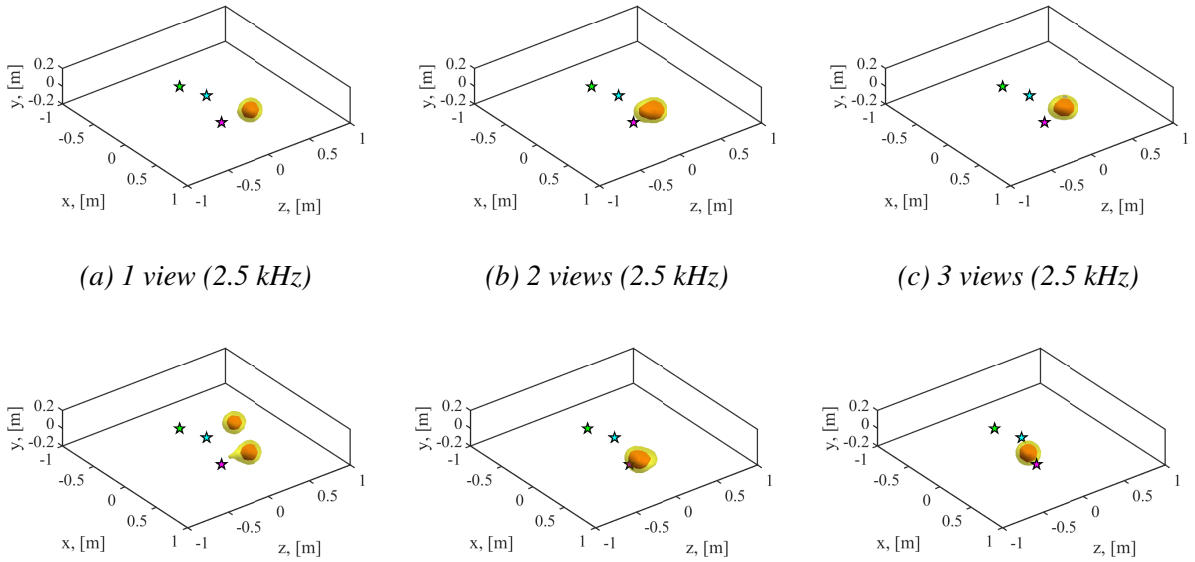

(a) 1 view (2.5 kHz) (b) 2 views (2.5 kHz) (c) 3 views (2.5 kHz)

(d) 1 view (5 kHz) (e) 2 views (5 kHz) (f) 3 views (5 kHz)

Figure 11: Three–dimensional acoustic source maps obtained for CLEAN–SC for a one–third–octave frequency band centered at 2.5 kHz (first row) and 5 kHz (second row).

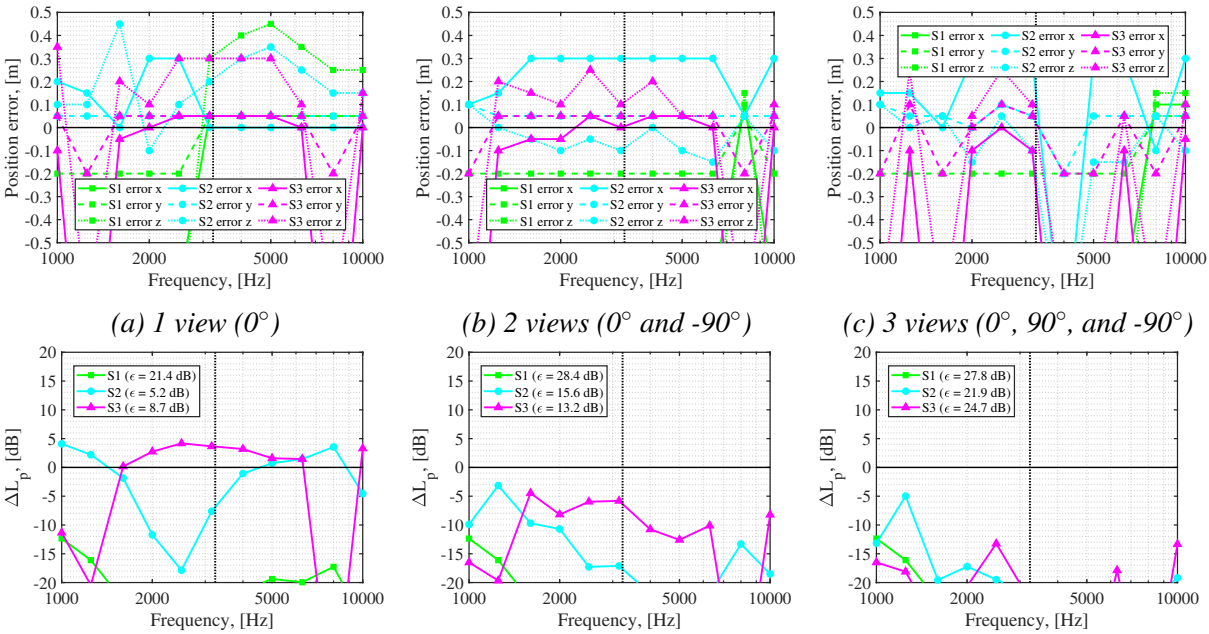

(a) 1 view (0°) (b) 2 views (0° and -90°) (c) 3 views (0°, 90°, and -90°)

(d) 1 view (0°) (e) 2 views (0° and -90°) (f) 3 views (0°, 90°, and -90°)

Figure 12: Relative errors in position in x, y, and z (first row) and L_p (second row) for each speaker made by CLEAN–SC. The vertical dotted line represents the Rayleigh resolution limit.

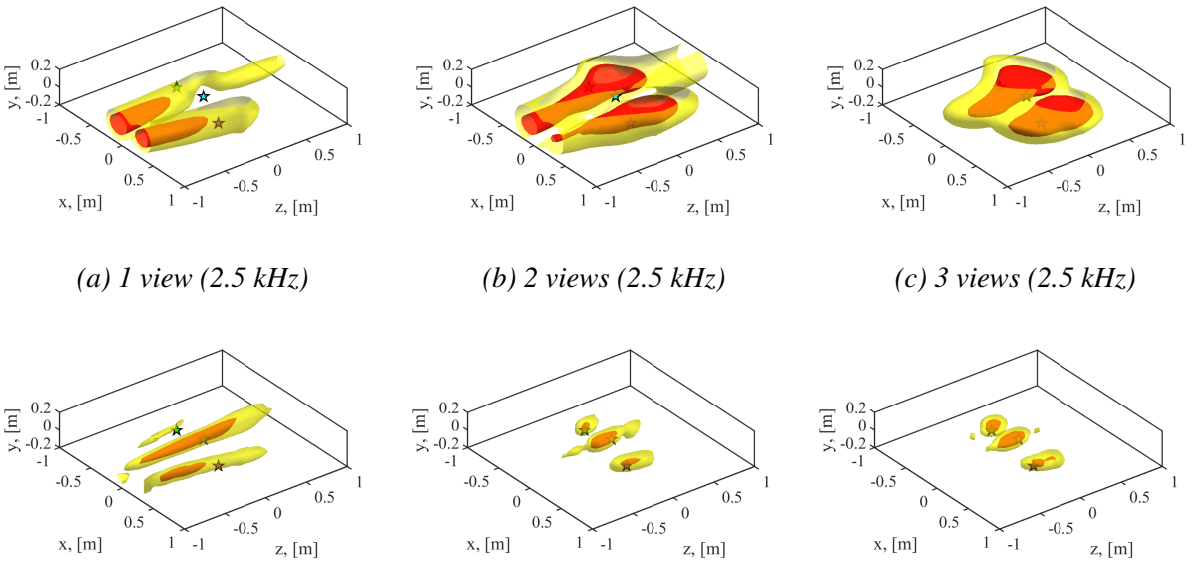

(a) 1 view (2.5 kHz) (b) 2 views (2.5 kHz) (c) 3 views (2.5 kHz)

(d) 1 view (5 kHz) (e) 2 views (5 kHz) (f) 3 views (5 kHz)

Figure 13: Three–dimensional acoustic source maps obtained for RL for a one–third–octave frequency band centered at 2.5 kHz (first row) and 5 kHz (second row).

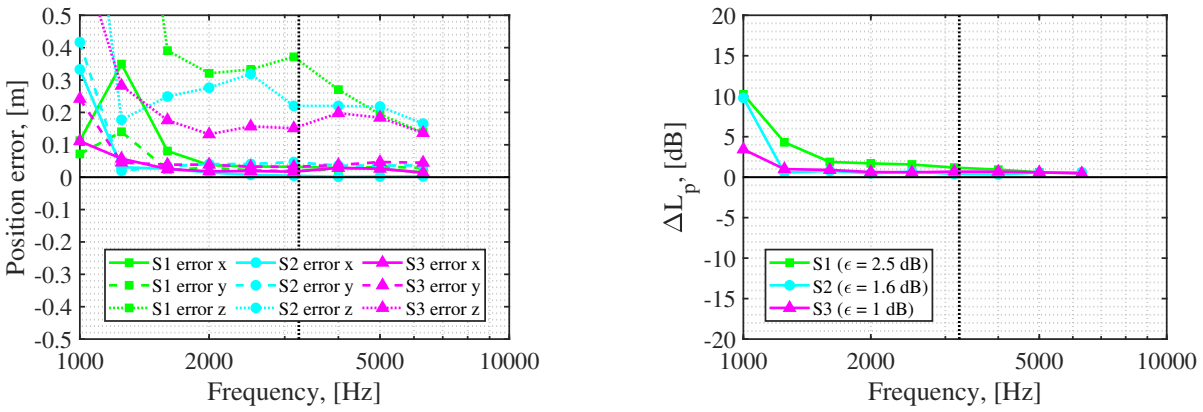

(a) (b)

Figure 14: Relative errors in position in x, y, and z (a) and L_p (b) for each speaker made by GO methods. The vertical dotted line represents the Rayleigh resolution limit. Adapted from [71].

investigated in terms of localization and quantification accuracy of sound sources.

A case study featuring three speakers emitting broadband incoherent noise in an anechoic chamber showed that the typical poor spatial resolution of planar arrays in the depth direction can be considerably improved by combining multiple asynchronous measurements with different array views, using the geometric average of their source autopowers. On the other hand, the

quantitative estimations of the frequency spectra in sound pressure level were found to be more accurate when a single view was employed in front of the speakers. Overall, FUNBF, RAB, and GO provided the best performance in terms of sound source localization, whereas CFDBF and GO provided the most accurate quantitative results in terms of sound pressure level spectra.

References

[1] S. Bartels, F. Márki, and U. Müller, *The influence of acoustical and non–acoustical factors on short–term annoyance due to aircraft noise in the field – The COSMA study,* Science of the Total Environment **538**, 834 (2015).

[2] R. Merino-Martinez, L. Bertsch, M. Snellen, and D. G. Simons, *Analysis of landing gear noise during approach,* in 22nd *AIAA/CEAS Aeroacoustics Conference, May 30 – June 1 2016, Lyon, France* (2016) AIAA paper 2016–2769.

[3] R. Merino-Martinez and M. Snellen, *Implementation of tonal cavity noise estimations in landing gear noise prediction models,* in 26th *AIAA/CEAS Aeroacoustics Conference, June 15 – 19 2020, Virtual Event* (2020) AIAA paper 2020–2578.

[4] S. Oerlemans, P. Sijtsma, and B. Méndez López, *Location and Quantification of Noise Sources on a Wind Turbine,* Journal of Sound and Vibration **299**, 869 (2007).

[5] R. Merino-Martinez, R. Pieren, and B. Schäffer, *Holistic approach to wind turbine noise: From blade trailing–edge modifications to annoyance estimation,* Renewable and Sustainable Energy Reviews **148**, 1 (2021).

[6] B. Barsikow, W. F. King III, and E. Pfizenmaier, *Wheel/Rail Noise Generated by a High–Speed Train Investigated with a Line Array of Microphones,* Journal of Sound and Vibration **118**, 99 (1987).

[7] U. Michel and B. Barsikow, *Localisation of sound sources on moving vehicles with microphone arrays,* in *Proceedings of EuroNoise 2003, May 19 – 21 2003, Naples, Italy*, paper ID 537 (2003).

[8] L. C. Caldas, P. C. Greco, C. C. J. Pagani, and L. A. Baccalá, *Comparison of different techniques for rotating beamforming at the university of São Paulo fan rig test facility,* in 6th *Berlin Beamforming Conference, February 29 – March 1 2016, Berlin, Germany* (GFaI, e.V., Berlin, 2016) BeBeC–2016–D14.

[9] R. Zamponi, P. Chiariotti, G. Battista, C. Schram, and P. Castellini, *3D Generalized Inverse Beamforming in wind tunnel aeroacoustic testing: application to a Counter Rotating Open Rotor aircraft model,* Applied Acoustics **163**, 1 (2020).

[10] R. Merino-Martinez, S. J. Heblij, D. H. T. Bergmans, M. Snellen, and D. G. Simons, *Improving Aircraft Noise Predictions by Considering the Fan Rotational Speed,* Journal of Aircraft **56**, 284 (2019).

[11] T. Mueller, *Aeroacoustic Measurements* (Springer Science & Business Media, Berlin, Germany, 2002) p. 313, ISBN: 978–3–642–07514–8.

[12] P. Sijtsma, *Phased array beamforming applied to wind tunnel and fly–over tests*, Tech. Rep. NLR–TP–2010–549 (National Aerospace Laboratory (NLR), Anthony Fokkerweg 2, 1059 CM Amsterdam, P.O. Box 90502, 1006 BM Amsterdam, The Netherlands, 2010).

[13] R. Merino-Martinez, *Microphone arrays for imaging of aerospace noise sources*, Ph.D. thesis, Delft University of Technology (2018), ISBN: 978–94–028–1301–2.

[14] R. Merino-Martinez, P. Sijtsma, M. Snellen, T. Ahlefeldt, J. Antoni, C. J. Bahr, D. Blacodon, D. Ernst, A. Finez, S. Funke, T. F. Geyer, S. Haxter, G. Herold, X. Huang, W. M. Humphreys, Q. Leclère, A. Malgoezar, U. Michel, T. Padois, A. Pereira, C. Picard, E. Sarradj, H. Siller, D. G. Simons, and C. Spehr, *A review of acoustic imaging methods using phased microphone arrays (part of the Aircraft Noise Generation and Assessment special issue), CEAS aeroacoustic journal*, CEAS Aeronautical Journal **10**, 197 (2019).

[15] P. Chiariotti, M. Martarelli, and P. Castellini, *Acoustic beamforming for noise source localization – Reviews, methodology and applications,* Mechanical Systems and Signal Processing **120**, 422 (2019).

[16] S. Luesutthiviboon, A. M. N. Malgoezar, R. Merino-Martinez, M. Snellen, P. Sijtsma, and D. G. Simons, *Enhanced HR–CLEAN–SC for resolving multiple closely spaced sound sources,* International Journal of Aeroacoustics **18**, 392 (2019).

[17] A. M. N. Malgoezar, M. Snellen, P. Sijtsma, and D. G. Simons, *Improving beamforming by optimization of acoustic array microphone positions,* in 6th *Berlin Beamforming Conference, February 29– March 1 2016, Berlin, Germany* (2016).

[18] M. C. Remillieux, E. D. Crede, H. E. Camargo, R. A. Burdisso, D. W. J., M. Rasnick, P. van Seeters, and A. Chou, *Calibration and Demonstration of the New Virginia Tech Anechoic Wind Tunnel,* in 14th *AIAA/CEAS Aeroacoustics Conference (*29th *AIAA Aeroacoustics Conference), May 5–7, 2008, Vancouver, British Columbia, Canada* (2008) AIAA paper 2008–2911.

[19] H. Holthusen, A. Bergmann, and P. Sijtsma, *Investigations and measures to improve the acoustic characteristics of the German–Dutch Wind Tunnel DNW–LLF,* in 18th *AIAA/CEAS Aeroacoustics Conference, 4 – 6 June 2012, Colorado Springs, USA* (2012) AIAA paper 2012–2176.

[20] J. Ocker and S. Tilgner, *The Porsche Wind Tunnel Microphone Array System,* in *Aachen Acoustics Colloquium, November 23 – 25, 2015, Aachen, Germany* (2015) pp. 135–151.

[21] C. J. Bahr, W. M. Humphreys, D. Ernst, T. Ahlefeldt, C. Spehr, A. Pereira, Q. Leclère, C. Picard, R. Porteus, D. J. Moreau, J. Fischer, and C. J. Doolan, *A comparison of microphone phased array methods applied to the study of airframe noise in wind tunnel testing,* in 23rd *AIAA/CEAS Aeroacoustics Conference, June 5 – 9 2017, Denver, CO, USA* (2017) AIAA paper 2017–3718.

[22] R. Merino-Martinez, M. P. J. Sanders, L. C. Caldas, F. Avallone, D. Ragni, L. D. de Santana, M. Snellen, and D. G. Simons, *Comparison between analog and digital microphone phased arrays for aeroacoustic measurements,* in 24th *AIAA/CEAS Aeroacoustics Conference, June 25 – 29 2018, Atlanta, Georgia, USA* (2018) AIAA paper 2018–2809.

[23] R. Merino-Martinez, E. Neri, M. Snellen, J. Kennedy, D. G. Simons, and G. J. Bennett, *Multi–approach study of nose landing gear noise,* Journal of Aircraft **57**, 517 (2020).

[24] R. Merino-Martinez, A. Rubio Carpio, L. T. Lima Pereira, S. van Herk, F. Avallone, M. Kotsonis, and D. Ragni, *Aeroacoustic design and characterization of the 3D–printed, open–jet, anechoic wind tunnel of Delft University of Technology,* Applied Acoustics **170**, 1 (2020).

[25] E. J. G. Arcondoulis, Y. Liu, P. Xu, and N. Chen, *An array pairing method for localizing distributed sources by acoustic beamforming,* Journal of the Acoustical Society of America – Express Letters **147**, E7 (2020).

[26] S. Oerlemans, *Detection of aeroacoustic sound sources on aircraft and wind turbines*, Ph.D. thesis, University of Twente, Enschede, the Netherlands (2009).

[27] Y. Zhou, V. Valeau, J. Marchal, F. Ollivier, and R. Marchiano, *Three–Dimensional identification of flow induced noise sources with a tunnel–shaped array of MEMS microphones,* Journal of Sound and Vibration **482**, 1 (2020).

[28] D. Evans, M. Hartmann, and J. Delfs, *Beamforming for point force surface sources in numerical data,* Journal of Sound and Vibration **458**, 303 (2019).

[29] R. Merino-Martinez, J. Kennedy, and G. J. Bennett, *Experimental study of realisitic low–noise technologies applied to a full-scale nose landing gear,* Aerospace Science and Technology **113**, 1 (2021).

[30] T. Geyer, E. Sarradj, and J. Giesler, *Application of a Beamforming Technique to the Measurement of Airfoil Leading Edge Noise,* Advances in Acoustics and Vibration **2012**, 1 (2012).

[31] D. Döbler, J. Ocker, and C. Puhle, *On 3D–beamforming in the wind tunnel,* in 6th *Berlin Beamforming Conference, February 29 – March 1 2016, Berlin, Germany* (GFaI, e.V., Berlin, 2016) BeBeC–2016–S10.

[32] T. F. Brooks and W. M. Humphreys, *Three–Dimensional Application of DAMAS Methodology for Aeroacoustic Noise Source Definition,* in 11th *AIAA/CEAS Aeroacoustics Conference, May 23 – 25 2005, Monterey, California, USA* (2005) AIAA paper 2005–2960.

[33] E. Sarradj, *Three–Dimensional Acoustic Source Mapping with Different Beamforming Steering Vector Formulations,* Advances in Acoustics and Vibration **2012**, 1 (2012).

[34] R. Porteous, Z. Prime, C. J. Doolan, and D. J. Moreau, *Three–dimensional beamforming of dipolar aeroacoustic sources,* Journal of Sound and Vibration **355**, 117 (2015).

[35] A. M. N. Malgoezar, M. Snellen, R. Merino-Martinez, D. G. Simons, and P. Sijtsma, *On the use of global optimization methods for acoustic source mapping,* Journal of the Acoustical Society of America **141**, 453 (2017).

[36] G. Battista, P. Chiariotti, M. Martarelli, and P. Castellini, *Inverse methods in aeroacoustic three–dimensional volumetric noise source localization and quantification,* Journal of Sound and Vibration **473**, 1 (20200).

[37] J. Hileman, B. Thurow, and M. Samimy, *Development and evaluation of a 3–D microphone array to locate individual acoustic sources in a high–speed jet,* Journal of Sound and Vibration **276**, 649 (2004).

[38] D. Ernst and C. Spehr, *Three–Dimensional Microphone Array for Wind Tunnel Application,* in 46th *International Congress and Exposition of Noise Control Engineering, 27–30 August, 2017, Hong Kong* (International Institute of Noise Control Engineering (I-INCE), 2017).

[39] T. Padois, O. Robin, and A. Berry, *3D source localization in a closed wind–tunnel using microphone arrays,* in 19th *AIAA/CEAS Aeroacoustics Conference, May 27 – 29 2013, Berlin, Germany* (2013) AIAA paper 2013–2213.

[40] P. Castellini and M. Martarelli, *Acoustic beamforming: Analysis of uncertainty and metrological performances,* Mechanical Systems and Signal Processing **22**, 672 (2008).

[41] G. Heilmann, D. Döbler, A. Meyer, and S. Barre, *Dynamic beamforming using moving phased arrays with integrated 3D scanners,* in 46th *International Congress and Exposition of Noise Control Engineering, 27–30 August, 2017, Hong Kong* (International Institute of Noise Control Engineering (I-INCE), 2017).

[42] L. K. Wächter, J. Ocker, D. Döbler, C. Puhle, and G. Herold, *Investigations on Beamforming in the Wind Tunnel Using Multiple Microphone Array Measurements,* in 7th *Berlin Beamforming Conference, March 5 – 6 2018, Berlin, Germany* (GFaI, e.V., Berlin, 2018) BeBeC–2018–S09.

[43] L. Yu, W. Jiang, J. Antoni, Q. Leclère, and H. Wu, *Acoustic Beamforming by Non–Synchronous Microphone Array Measurements,* in 7th *Berlin Beamforming Conference, March 5 – 6 2018, Berlin, Germany* (GFaI, e.V., Berlin, 2018) BeBeC–2018–S10.

[44] N. Chu, Y. Ning, L. Yu, Q. Huang, and D. Wu, *A High–Resolution and Low–Frequency Acoustic Beamforming Based on Bayesian Inference and Non–Synchronous Measurements,* IEEE Access **8**, 82500 (2020).

[45] L. T. Lima Pereira, R. Merino-Martinez, D. Ragni, D. Gómez-Ariza, and M. Snellen, *Combining asynchronous microphone array measurements for enhanced acoustic imaging and volumetric source mapping,* Applied Acoustics **182**, 1 (2021).

[46] F. Ning, J. Song, J. Hu, and J. Wei, *Sound source localization of non–synchronous measurements beamforming with block Hermitian matrix completion,* Mechanical Systems and Signal Processing **147**, 1 (2020).

[47] E. Sarradj, G. Herold, P. Sijtsma, R. Merino-Martinez, A. M. N. Malgoezar, M. Snellen, T. F. Geyer, C. J. Bahr, R. Porteous, D. J. Moreau, and C. J. Doolan, *A microphone array method benchmarking exercise using synthesized input data,* in 23rd *AIAA/CEAS Aeroacoustics Conference, June 5 – 9 2017, Denver, CO, USA* (2017) AIAA paper 2017–3719.

[48] R. Merino-Martinez, P. Sijtsma, and M. Snellen, *Inverse Integration Method for Distributed Sound Sources,* in 7th *Berlin Beamforming Conference, March 5 – 6 2018, Berlin, Germany* (GFaI, e.V., Berlin, 2018) BeBeC–2018–S07.

[49] R. Merino-Martinez, P. Sijtsma, A. Rubio Carpio, R. Zamponi, S. Luesutthiviboon, A. M. N. Malgoezar, M. Snellen, C. Schram, and D. G. Simons, *Integration methods for distributed sound sources,* International Journal of Aeroacoustics **18**, 444 (2019).

[50] R. Merino-Martinez, S. Luesutthiviboon, R. Zamponi, A. Rubio Carpio, D. Ragni, P. Sijtsma, M. Snellen, and C. Schram, *Assessment of the accuracy of microphone array methods for aeroacoustic measurements,* Journal of Sound and Vibration **470**, 1 (2020).

[51] R. Merino-Martinez, G. Herold, M. Snellen, and R. P. Dougherty, *Assessment and comparison of the performance of functional projection beamforming for aeroacoustic measurements,* in 8th *Berlin Beamforming Conference, March 2 – 3 2020, Berlin, Germany* (GFaI, e.V., Berlin, 2020) BeBeC–2020–S7.

[52] B. D. van Veen and K. M. Buckley, *Beamforming: A Versatile Approach to Spatial Filtering,* IEEE ASSP Magazine **5**, 4 (1988).

[53] R. P. Dougherty, *Functional Beamforming,* in 5th *Berlin Beamforming Conference, February 19 – 20 2014, Berlin, Germany* (GFaI, e.V., Berlin, 2014) BeBeC–2014–01.

[54] R. Merino-Martinez, M. Snellen, and D. G. Simons, *Functional beamforming applied to imaging of flyover noise on landing aircraft,* Journal of Aircraft **53**, 1830 (2016).

[55] R. Merino-Martinez, M. Snellen, and D. G. Simons, *Functional Beamforming Applied to Full Scale Landing Aircraft,* in 6th *Berlin Beamforming Conference, February 29 – March 1 2016, Berlin, Germany* (GFaI, e.V., Berlin, 2016) BeBeC–2016–D12.

[56] E. Sarradj, *A fast signal subspace approach for the determination of absolute levels from phased microphone array measurements,* Journal of Sound and Vibration **329**, 1553 (2010).

[57] H. Cox, R. Zeskind, and M. Owen, *Robust adaptive beamforming,* IEEE Transactions on Acoustics Speech and Signal Processing **ASSP–35**, 1365 (1987).

[58] O. L. Frost, *An algorithm for linearly constrained adaptive array processing,* Proceedings of the IEEE **60**, 926 (1972).

[59] X. Huang, L. Bai, I. Vinogradov, and E. Peers, *Adaptive beamforming for array signal processing in aeroacoustic measurements,* Journal of the Acoustical Society of America **131**, 2152 (2012).

[60] P. Sijtsma, *CLEAN based on spatial source coherence,* International Journal of Aeroacoustics **6**, 357 (2007), SAGE Publications Ltd. London, United Kingdom.

[61] P. Sijtsma, R. Merino-Martinez, A. M. N. Malgoezar, and M. Snellen, *High–Resolution CLEAN–SC: Theory and Experimental Validation,* International Journal of Aeroacoustics **16**, 274 (2017), SAGE Publications Ltd. London, United Kingdom.

[62] W. H. Richardson, *Bayesian–Based Iterative Method of Image Restoration,* Journal of the Optical Society of America **62**, 55 (1972).

[63] L. B. Lucy, *An iterative technique for the rectification of observed distributions,* The Astronomical Journal **79**, 745 (1974).

[64] D. Papamoschou, *Imaging of Distributed Directional Noise Sources,* Journal of Sound and Vibration **330**, 2265 (2011).

[65] E. Tiana-Roig and F. Jacobsen, *Deconvolution for the localization of sound sources using a circular microphone array,* The Journal of the Acoustical Society of America **134**, 2078 (2013).

[66] T. C. Yang, *On conventional beamforming and deconvolution,* in *OCEANS 2016 – Shanghai* (2016) pp. 1–5.

[67] D. Papamoschou, D. Morata, and P. Shah, *Inverse Acoustic Methodology for Continuous-Scan Phased Arrays,* AIAA Journal **57**, 5126 (2019).

[68] D. Morata and D. Papamoschou, *Advances in the direct spectral estimation of aeroacoustic sources using continuous-scan phased arrays, AIAA Scitech 2021 Forum*, 10.2514/6.2021-0215.

[69] T. F. Brooks and W. M. Humphreys, *A Deconvolution Approach for the Mapping of Acoustic Sources (DAMAS) determined from phased microphone arrays,* in 10^{th} *AIAA/CEAS Aeroacoustics Conference, May 10 – 12 2004, Manchester, UK* (2004) AIAA paper 2004–2954.

[70] D. Morata and D. Papamoschou, *Extension of Traditional Beamforming Methods to the Continuous–Scan Paradigm,* in 14^{th} *AIAA SciTech Forum, January 3 – 7, 2022, San Diego, CA, USA* (2022) AIAA paper 2022–1154.

[71] B. von den Hoff, R. Merino-Martinez, M. Snellen, and D. Simons, *Using global optimization methods for three–dimensional localization and quantification of incoherent acoustic sources,* Journal of the Acoustical Society of America (Express Letter) **2**, 1 (2022).

[72] C. B. Goates, B. M. Harker, T. B. Neilsen, and K. L. Gee, *Extending the bandwidth of an acoustic beamforming array using phase unwrapping and array interpolation,* The Journal of the Acoustical Society of America **141**, EL407 (2017).

[73] L. Yu, J. Antoni, Q. Leclère, and W. Jiang, *Acoustic source reconstruction from non–synchronous sequential measurements by Fast Iterative Shrinkage Thresholding Algorithm,* Journal of Sound and Vibration **408**, 351 (2017).

[74] Visaton – Speaker FRWS 5 – 8 Ohm, *https://www.visaton.de/en/products/drivers/fullrange-systems/frws-5-8-ohm,* Accessed in May 2022.

[75] CAE Systems website, *https://www.cae-systems.de/en/products/acoustic-camera-sound-source-localization/bionic-m-112.html,* Accessed in January 2017.

[76] R. Merino-Martinez, E. Neri, M. Snellen, J. Kennedy, D. G. Simons, and G. J. Bennett, *Analysis of nose landing gear noise comparing numerical computations, prediction models and flyover and wind–tunnel measurements,* in 24th *AIAA/CEAS Aeroacoustics Conference, June 25 – 29 2018, Atlanta, Georgia, USA* (2018) AIAA paper 2018–3299.